Chaos in the Relativistic Three-Body Problem

Jared Stephens Jay

A senior thesis submitted to the faculty of
Brigham Young University
in partial fulfillment of the requirements for the degree of

Bachelor of Science

David Neilsen, Advisor

Department of Physics and Astronomy

Brigham Young University

April 2015

ABSTRACT

Chaos in the Relativistic Three-Body Problem

Jared Stephens Jay
Department of Physics and Astronomy, BYU
Bachelor of Science

We study the chaotic properties of the three-body problem in general relativity and examine the effects of successive post-Newtonian Hamiltonian correction terms. We set up a planar, two-parameter, three-body system consisting of a circular binary and an incoming star, and integrate the system many times, varying the two initial parameters by small amounts. We study the cases of equal masses and unequal masses. We observe that the initial parameter space contains regions of fairly predictable behavior and regions of chaotic behavior at all levels of approximation to relativity. This is strong evidence that the three-body exhibits the same chaos in general relativity as in Newtonian gravity.

Keywords: chaos, relativity, three-body

ACKNOWLEDGMENTS

I would like to thank the Brigham Young University Department of Physics and Astronomy for supporting me in this research, and the Fulton Supercomputing Laboratory for allowing me to use their hardware to do the large-scale simulations of three-body interactions. I also thank my advisor Dr. David Neilsen for mentoring me throughout the entire research process.

This thesis is based upon work supported by the National Science Foundation under Grant NSF PHY-1308727 to Brigham Young University.

Contents

List of Figures

Chapter 1

Introduction

1.1 The Three-Body Problem

The gravitational three-body problem has been an important area of research since the time of Newton. The problem is to find the positions and velocities of three gravitationally interacting objects at every future moment in time given the initial positions and velocities of each object. Newton treated this problem in his book *Principia Mathematica* to try and understand the Earth-Moon-Sun system, but was unable to find a solution.

Over the space of many years, scores of scientists and mathematicians tried to solve this problem [1, 2], including Euler, Clairaut, and Lagrange. In 1887, Poincare proved that there is no general analytical solution in terms of algebraic operations and integrals, putting an end to all attempts to solve the problem analytically. (An analytic power series solution was developed afterwards, but it converges so slowly that it has no practical application [1].)

In the early twentieth century, Einstein developed general relativity, a geometric model of gravity. This new model of gravity provides additional complications to the three-body problem that we wish to investigate. Instead of solving the full Einstein equations, we use a perturbation

approach on the Hamiltonian for the Newtonian three-body problem called the post-Newtonian approximation. The

1.2 Chaos

The main focus of our research is the presence of chaos in the three-body problem. Chaos was first observed in the twentieth century in connection with the weather. The typical example is the butterfly effect, in which a butterfly flapping its wings in Argentina can cause a tornado to occur sometime in the future in Texas. The defining property of chaos in a physical system is that an arbitrarily small change in the initial conditions can cause an arbitrarily large difference in the outcome of an interaction.

The Newtonian three-body system is now known to exhibit deterministic chaos [1]. This means the problem is deterministic by Newton's laws, yet in most cases the initial conditions can't possibly be measured precisely enough to give reliable long-term predictions. The chaos in the three-body problem has been studied extensively in Newtonian gravity [3], but little research has been done on the chaos of the three-body system in general relativity.

1.3 Research and Motivation

The purpose of our research is to analyze the chaotic behavior of the three-body problem in general relativity, and examine the effects of the post-Newtonian Hamiltonian correction terms on the dynamics of the system. This knowledge will have applicability in future numerical simulations of celestial bodies and may help us gain a greater understanding of black hole formation. Most black holes are formed in clusters of stars, and some believe that the chaotic effects of this many-body system causes the black holes to form more quickly than expected through multiple two-body mergers [17, 18]. The code that we have developed in this project could be expanded to this type

of problem.

Another application of recent interest is the stability of distant solar systems. The Kepler Space Telescope has identified over a thousand planets orbiting distant stars [4]. Scientists have been running simulations to test the stability of these orbits in Newtonian gravity. We would like to know if general relativity causes instabilities not seen in Newtonian gravity. We are currently working to adapt our code to this project.

1.4 Previous Work

Our research builds mainly on work done by P. Boyd and S. McMillan on chaos in the Newtonian three-body problem [5]. In their paper, they restricted the three-body problem to a simple setup involving a binary and an incoming star and then integrated the equations of motion until one of the objects escaped the system. We follow the same approach in our research. This allows us to check our results against previously established results.

In 2007, David Tanner extended the investigation to general relativity [6] using a Hamiltonian formalism of the post-Newtonian equations developed by Schäfer [7] (see corrections in Lousto et al [8].). Tanner extended Boyd and McMillan's simulations to second-order post-Newtonian (PN2). However, an error in the computer code was discovered after his thesis was completed. J.J. Campbell later repeated Tanner's work with corrections up to first-order post-Newtonian (PN1) [9].

Significant work was done on numerical simulations of three bodies in relativity by Galaviz [10], who included 2.5-order post Newtonian for the first time (PN2.5). Our methods of numerical integration are similar to his, but applied to the system studied by Boyd and McMillan to study the chaos of the system.

1.5 Outline

In this thesis we report a successful extension of Boyd and McMillan's research to post-Newtonian orders PN2 and PN2.5. We have examined the characteristics and effects of each order of approximation and we have observed that the system is chaotic at all orders.

In Chapter 2 we explain in detail the methods we used to analyze the problem. We start by explaining the post-Newtonian approximation that we use. We then choose a special case of the three-body problem and derive the initial conditions analytically. We explain our method of numerical integration (LSODA) and give evidence of its validity with special tests. In Chapter 3 we present the results of the simulations in the form of color-coded images. We point out the characteristics of chaos and explain unexpected effects in the images. In Appendix A we have included the full post-Newtonian Hamiltonians.

Chapter 2

Methods

2.1 Post-Newtonian Approximation

Due to the large number of simulations involved in our study of chaos, we do not solve the full Einstein equations; instead, we assume weak gravitational fields and use a perturbation approach. We assume $(v/c)^2 \ll 1$ and $GM/r \ll 1$, where v is velocity, c is the speed of light, and GM/r is the Newtonian gravitational potential. We then find correction terms to the Newtonian Hamiltonian. The Hamiltonian is expanded in the form

$$H = H_N + c^{-2}H_{PN1} + c^{-4}H_{PN2} + c^{-5}H_{PN2.5}, \tag{2.1}$$

where H_N is the Newtonian Hamiltonian. The terms H_{PN1}, H_{PN2}, and $H_{PN2.5}$ represent successive post-Newtonian approximations to general relativity. We refer to each order of approximation respectively as zeroth-order post-Newtonian (PN0), first-order post-Newtonian (PN1), second-order post-Newtonian (PN2) and two-and-a-half-order post-Newtonian (PN2.5). The Hamiltonian $H_{2.5PN}$ is a dissipative term that includes the first gravitational wave emission effects. Part of the purpose of our research is to discover the properties of each of the available orders of approximation to general relativity up to PN2.5. Hamiltonians of this form above order PN2.5 have not yet

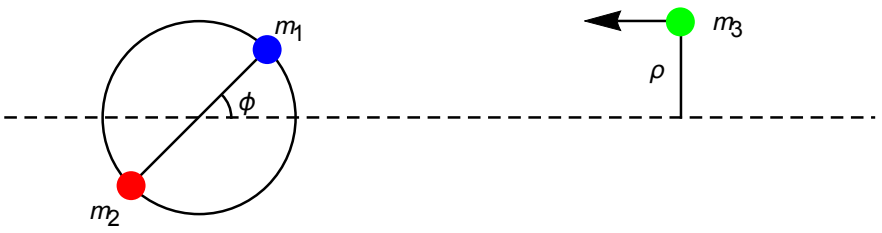

Figure 2.1 The initial conditions of our simulations depend on only two parameters: the impact parameter ρ, which is the perpendicular distance of the third object from the x-axis, and the phase angle ϕ, which is the initial inclination of the binary from the x-axis. The masses of the objects are m_1, m_2, and m_3. The objects are color-coded, and the colors are consistent throughout the document.

been derived for three bodies. We examine the effects of each of these terms on the trajectories in our simulations.

These Hamiltonian approximations are very complicated and have been successfully derived for three bodies up to PN2.5 by Schäfer et al [7, 11] with corrections by Lousto et al [8]. For order PN2.5 we used the form of the Hamiltonian given by Galaviz [10]. The Hamiltonians are displayed in Appendix A.

Hamilton's equations express the time derivatives of the position and momentum of the objects,

$$\dot{x}^i_a = \frac{\partial H}{\partial p^i_a}, \tag{2.2}$$

$$\dot{p}^i_a = -\frac{\partial H}{\partial x^i_a}, \tag{2.3}$$

where i labels the axis and a labels the object. These form a set of eighteen ordinary differential equations which can be numerically integrated from initial conditions to determine the motion of the three objects.

2.2 Initial Conditions

We limit our experiments to single-star binary interactions, in which two objects are initially in a circular orbit, and a third object approaches from a large distance before interacting with the binary. The system is restricted to a plane, with the third object initially moving in the negative x-direction. The initial conditions for each run require only two parameters: ϕ, the initial phase of the binary relative to the x-axis, and ρ, the impact parameter in units of r, the radius of the binary. The initial diameter of the binary and the velocity of the incoming object were identical in all of our simulations.

The initial conditions for the circular binary are found in the same way for all the post-Newtonian orders we work with, the only difference being the form of the Hamiltonian. We give an example here using the Newtonian Hamiltonian

$$H = \frac{p_1^2}{2m_1} + \frac{p_2^2}{2m_2} - \frac{Gm_1m_2}{|x_2 - x_1|}, \tag{2.4}$$

where p_1 and p_2 are the momenta of the two objects, m_1 and m_2 are the masses, x_1 and x_2 are the positions, and G is the gravitational constant.

We restrict ourselves to the center-of-mass frame where $p_1 = -p_2$ and we let $p = \frac{p_1}{\mu}$ and $q = |x_2 - x_1|/GM$ where $M = m_1 + m_2$ and $\mu = m_1m_2/(m_1 + m_2)$ is the reduced mass. The Hamiltonian then simplifies to

$$H = \mu\frac{p^2}{2} - \frac{\mu}{q}. \tag{2.5}$$

We now define a new scaled Hamiltonian

$$\hat{H} = \frac{H}{\mu} = \frac{p^2}{2} - \frac{1}{q}. \tag{2.6}$$

Two-body Hamiltonians of this form can be found up to order PN3 in Schäfer [12].

The angular momentum is defined by $j = qp_\phi$. For circular orbits, we have $p = p_\phi$, so we can

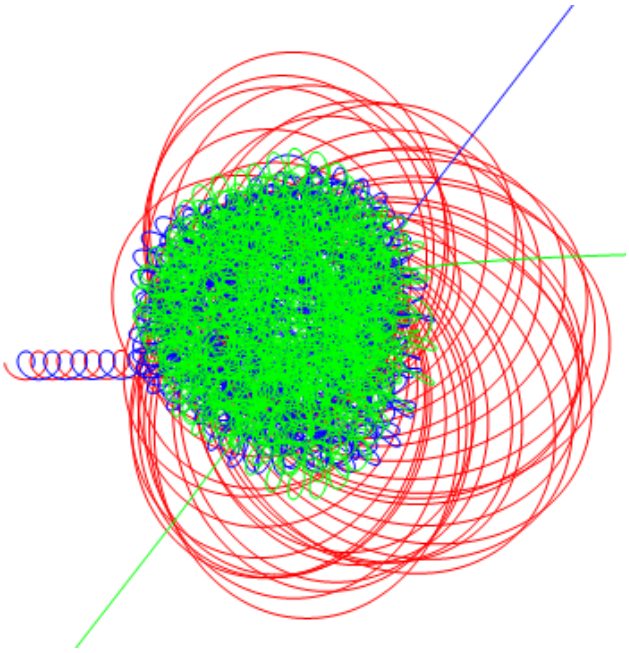

Figure 2.2 A quasi-periodic interaction between all three bodies called a resonance.

replace each p in the Hamiltonian with $\frac{j}{q}$,

$$\hat{H} = \frac{j^2}{2q^2} - \frac{1}{q}. \tag{2.7}$$

With everything is in terms of q, we can take the partial derivative of this Hamiltonian with respect to q. The condition for a circular orbit is $p_r = 0$. We therefore require

$$\dot{p}_r = -\frac{\partial H}{\partial q} = \frac{j^2}{q^3} - \frac{1}{q^2} = 0. \tag{2.8}$$

The solution to this equation is $j = \sqrt{q}$, which means $p = \frac{j}{q} = \frac{1}{\sqrt{q}}$. The total momentum of the first object is then given by scaling back to our original units, $p_1 = \mu p$. The initial conditions for other PN orders are calculated analogously.

The third object is initially far to the right at a distance of $60r$ from the center of the binary. We choose the initial incoming velocity of the third object such that the total energy of the three-body system is less than zero. It can be shown, following Boyd and McMillan [5], that this velocity must

satisfy

$$v < \sqrt{\frac{Gm_1m_2(m_1+m_2+m_3)}{2rm_3(m_1+m_2)}}. \tag{2.9}$$

We arbitrarily set the object's velocity to one-half this value in the $-x$ direction (approaching the binary).

Setting the total energy to be less than zero guarantees that at least two of the objects will be in a bound state at the end of a run. This restriction limits the possible outcomes of each experiment to the following four: (1) a flyby, when the third object simply flies by the binary, (2) an exchange, when the third object takes the place of one of the objects in the binary, (3) a collision, or (4) resonance, which is a complicated interaction like that shown in Fig. 2.2.

The plots in this thesis use a consistent color scheme, in which the color of a pixel represents which of the three objects escaped the system. Blue represents m_1, red represents m_2, and green represents m_3, as in figure 2.1. Here, and often throughout this document, we refer to the objects themselves by their masses m_i.

2.3 Numerical Methods

In our computations we use geometric units, where the Gravitational constant $G = 1$ and the speed of light $c = 1$. In order to return to SI units, we multiply geometric quantities by the derived conversion factors $R = \frac{GM}{c^2}$ and $T = \frac{GM}{c^3}$, where M is any mass scaling factor we desire.

We generate Eqs. (2.2) and (2.3) in Mathematica and integrate them in FORTRAN on Marylou7, the supercomputer at Brigham Young University. We use an integrator called LSODA, which is twelfth-order integrator with adaptive step size [13, 14]. The adaptive time stepping is crucial in our scattering experiments. LSODA runs either an Adams-Moulton or a Gear method depending on the stiffness of the problem. In the following sections we review the tests we have done with this integrator to prove its accuracy.

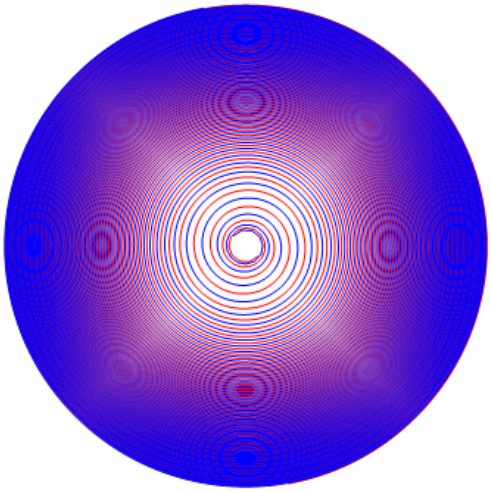

Figure 2.3 Simulation of a binary in-spiral due to emission of gravitational waves.

2.3.1 Error in Conserved Quantities

A good test of the validity of our simulations is to check that the values of the Hamiltonian and the angular momentum for the system are conserved. We calculate the Hamiltonian at the beginning and the end of each simulation and find the relative error given by the formula $(H_f - H_i)/H_i$. The error in Newtonian gravity never exceeds 1.3×10^{-5}.

We test for conservation of angular momentum in the same way. Our tests show that the relative error in the total angular momentum is around 10^{-9} or smaller everywhere, provided the initial angular momentum is not zero.

2.3.2 Gravitational Waves

When gravitational wave emission is included in the simulation at order PN2.5, the objects lose energy to gravitational waves and gradually spiral inward until they converge or coalesce. The theoretically predicted time τ for coalesence of a circular binary is given by

$$\tau = \frac{5}{256} \frac{c^5 R_0^4}{G^3 (m_1 + m_2)^2 \mu}, \tag{2.10}$$

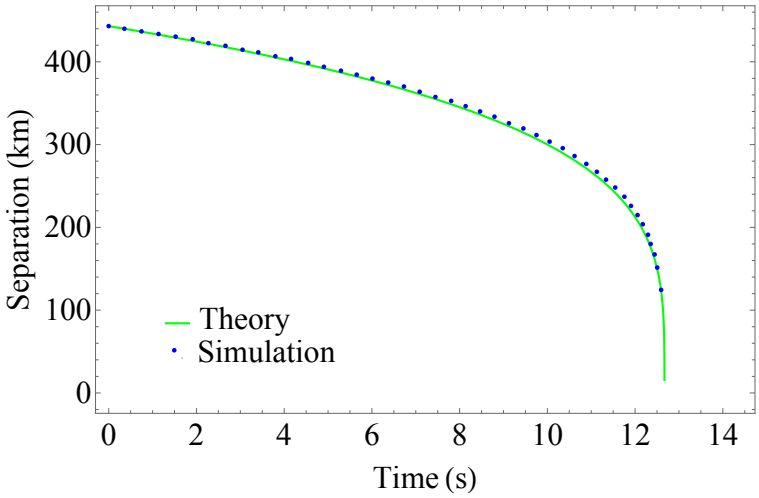

Figure 2.4 Relative separation over time between the two bodies in the binary according to theory (green line) and our simulation (blue dots). The bodies lose energy over time through the emission of gravitational waves and gradually spiral in towards each other.

where R_0 is the initial diameter of the binary and μ is the reduced mass [15].

Figures 2.3 and 2.4 show the results of our simulation of two bodies of equal mass, initially in a circular orbit of radius 50 geometric units, that spiral inward due to gravitational wave emission in PN2.5 gravity. Figure 2.3 shows the actual paths the two bodies followed. Figure 2.4 is a plot of the relative separation between two bodies (blue dots) versus time with a comparison to the theoretical prediction (green line). The curve predicted by theory is

$$R(t) = R_o\left(\frac{\tau - t}{\tau - t_o}\right)^{1/4} \tag{2.11}$$

and it closely matches our simulation. The coordinate time is not gauge invariant in general relativity, and has been scaled to match the theoretical inspiral time.

2.3.3 Long Runs

In Newtonian gravity, two objects in a circular orbit should maintain that same orbit forever. We tested our code in this situation and found that a circular orbit increased its radius by about 0.1% after more than 750,000 orbits.

Thus, we have tested the ability of the code to conserve energy and angular momentum. We have shown that it reproduces the correct inspiral solution for bodies emitting gravitational waves. Finally, we have shown that it maintains a fixed orbital configuration for relatively long times. We conclude that the code is capable of giving valid results for our scattering experiments.

Chapter 3

Results

3.1 Scattering in the Three-Body Problem

In this chapter we present the results of our simulations. The results come in three types: (1) equal mass scattering, (2) non-equal mass scattering, and (3) quasi-periodic runs. For the equal mass binaries, all three objects have the same mass. We run these binaries at orders PN0, PN1, PN2, and PN2.5, and plot the outcomes over the initial parameter space of ρ and ϕ. As we zoom in on these plots, the features of chaos are evident. For the non-equal mass binaries, we perform the same simulations, but the mass of m_1 is increased. We explain some unexpected effects of the increased mass, such as strange symmetries and perfect alignment in the plots. We then examine a few long-lived runs that exhibited quasi-periodic behavior.

3.2 Visualizing Chaos

In order to observe chaos, we set up thousands of runs using the methods outlined in Chapter 2 and vary the two parameters ρ and ϕ by small amounts. To visualize the results of all these runs on a two-dimensional image, we plot which of the three objects escaped the system versus the

initial parameters ρ and ϕ. Each object has been color-coded for these plots: red is m_1, blue is m_2, and green is m_3, where m_1 and m_2 form the initial binary and m_3, comes in from infinity. For a chaotic system, we expect to see the colors switch erratically over very small ranges in the initial parameters.

3.3 Equal Mass Scattering

The results of the simulations are plotted in Fig. 3.1. Each pixel represents the outcome of a simulation initialized with certain values of ρ and ϕ, where $-10r \leq \rho \leq 14r$ and $0 \leq \phi \leq \pi$. Because of the symmetry of the equal-mass binary, these ranges for the initial parameters cover the whole space of interactions, excluding distant flybys. The color of each pixel indicates which object escapes the system. The black pixels correspond to simulations that result in a collision or black hole merger. A black hole merger occurs when the separation between particles is less than the sum of their Schwarzschild radii. The regions of solid color are areas of relative predictability, where a change in the initial parameters has little effect on the final outcome. The fuzzy regions correspond to chaotic behavior where very small variations in the initial parameters give large differences in the outcome. For large values of ρ, the third object simply flies by the binary without any complicated interaction, as should be expected.

When we add the first-order post-Newtonian corrections (top-right of Fig. 3.1) to the Hamiltonian, we see a similar picture but with a phase shift (the whole image is shifted to the left). By experiment, we have discovered that this phase shift occurs because the binary rotates more quickly. There are interesting changes to the interior of the image as well, most notably the lack of black pixels and less chaotic fuzz. We have observed that at this level of approximation to general relativity, when the objects get too close together they feel a rapidly increasing repulsive force which causes them to fly apart very quickly. This makes collisions rare, so there are very few black

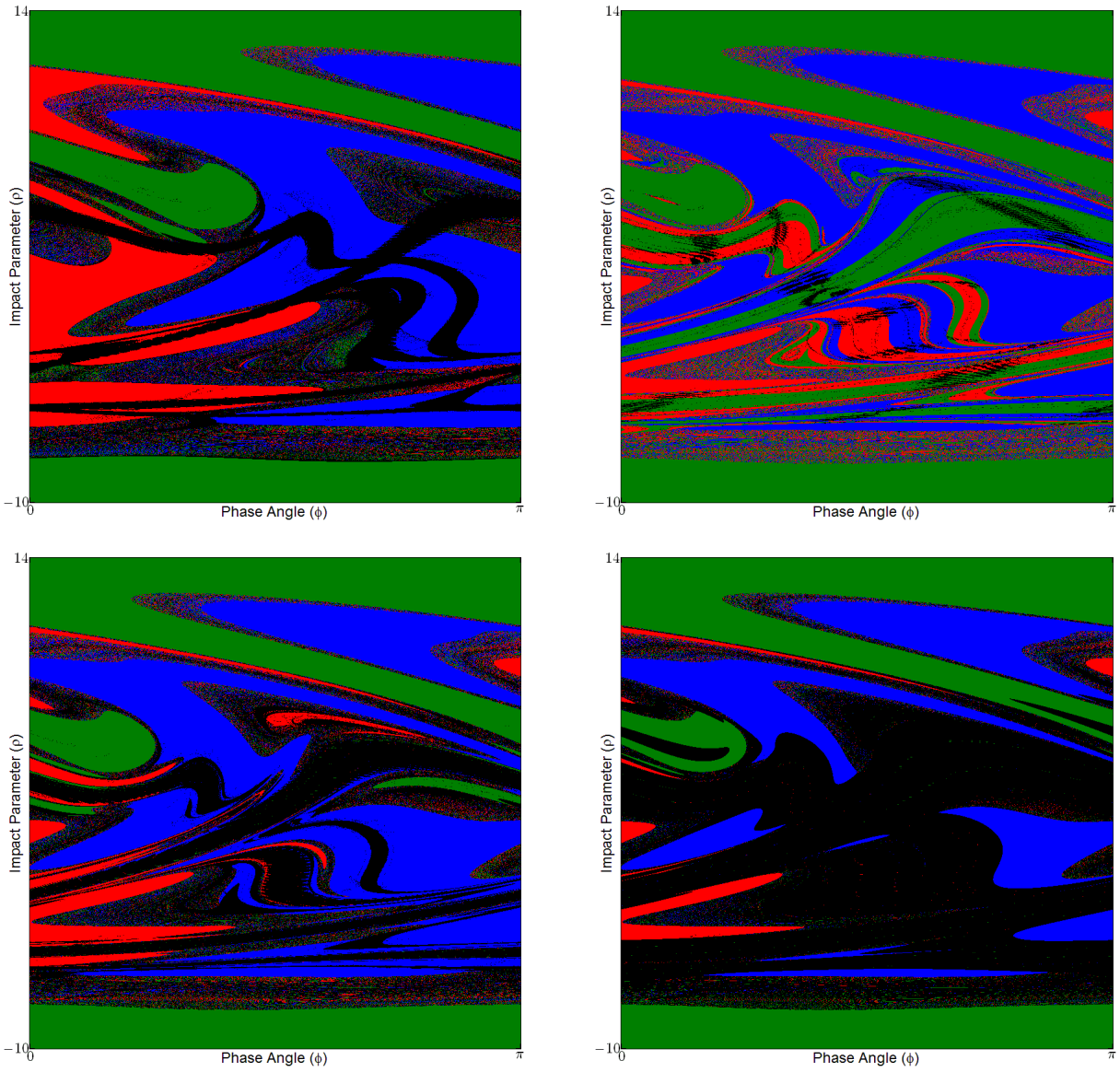

Figure 3.1 Each pixel in this figure represents the outcome of a simulation with initial parameters ρ and ϕ. The color indicates which of the three bodies escaped from the other two. Black pixels are collisions. This figure shows the results of orders PN0 (top-left), PN1 (top-right), PN2 (bottom-left), and PN2.5 (bottom-right). The fuzzy regions correspond to chaotic behavior.

pixels in the image. It also causes many close encounters to result in the bodies flying apart instead of following chaotic orbits, so there is less fuzziness in some areas.

We have deduced by experiments that this effect is caused by the first two terms in the second sum in the first-order correction Hamiltonian H_{PN1} (see Appendix A), except for one of the seven $\mathbf{p}_a \cdot \mathbf{p}_b$ terms. This is the minimal part of the Hamiltonian that must be removed to eliminate the repulsion effect. We will call this repulsive part H_{rep},

$$H_{rep} = -\frac{1}{4} \sum_{a,b \neq a} \frac{m_a m_b}{r_{ab}} \left\{ 6\frac{p_a^2}{m_a^2} - 6\frac{\mathbf{p}_a \cdot \mathbf{p}_b}{m_a m_b} \right\}. \tag{3.1}$$

For two equal masses, this simplifies to

$$H_{rep} = -\frac{3}{2r_{12}} (\mathbf{p}_1 - \mathbf{p}_2) \cdot (\mathbf{p}_1 - \mathbf{p}_2). \tag{3.2}$$

In the center of momentum frame ($p = p_1 = -p_2$), this can be written as

$$H_{rep} = -\frac{6}{r_{12}} p^2. \tag{3.3}$$

Now it is easier to see why the objects fly apart. Since p_1^2 is proportional to the kinetic energy of one body on average, by the virial theorem, it tends to vary inversely with the potential energy, which goes as $1/r_{12}$. So $H_{rep} \propto 1/r_{12}^3$. When the objects get too close, this part of the Hamiltonian blows up much more rapidly than the other parts. Simulations at order PN1 are therefore unphysical for close interactions.

The second-order corrections (bottom-left of Fig. 3.1) counteract some of the strange effects of the first-order corrections. The black space, which indicates mergers or collistions of two objects, has returned because the Hamiltonian has terms of higher order that overpower the repulsion from H_{rep}.

Adding the 2.5-order corrections (bottom-right of Fig. 3.1) greatly increases the black space. This is explained by gravitational wave emission, which is now included at this order of approximation to general relativity. This emission reduces the energy of the bodies and causes them to

fall inward more quickly, and thus they collide in many more cases. This effect can be seen in the binary tests in the section on gravitational waves in this paper.

The overall shape of the plots is the same at each PN order. Chaotic regions are visible at every order. The regions where the plots differ are often in areas where the post-Newtonian expansion becomes unphysical, as we showed in the case of PN1, because interactions in those regions include close approaches in which $(v/c)^2$ is not small.

When we zoom in on each of the images shown, we begin to see scale-invariance, a distinguishing feature of chaos. In Fig. 3.2, we show successive zooms for each of the orders PN0, PN1, PN2, and PN2.5. Each successive image is zoomed 400 times more than the previous one. The solutions show the same features at every level of zoom, regions of continuous color broken by fuzzy bands where the solution is chaotic. The scale-invariance seen in the plots results from chaos. In the last image of each column, the impact parameter ρ covers a range of only 1.5×10^{-4} times the radius of the binary, and the phase angle ϕ covers a range of only $6.25\pi \times 10^{-6}$ radians. The wide variety of outcomes in this tiny area is strong evidence that the three-body problem is chaotic in both Newtonian and relativisitic gravity.

3.4 Non-Equal Mass Scattering

In addition to studying the interactions of three bodies of equal mass, we examined the effects that arise from changing the mass of one of the objects in the system. The object we chose was m_1, a member of the initial binary. We ran the same simulations as before, but with the mass of m_1 increased to 2, 3, 5, and 10 times its original mass. The outcomes of these simulations are shown all together in figure 10. Notice that the phase angle ϕ now runs all the way to 2π. The new asymmetry of the binary makes this extension necessary in order to see all of the possible interactions.

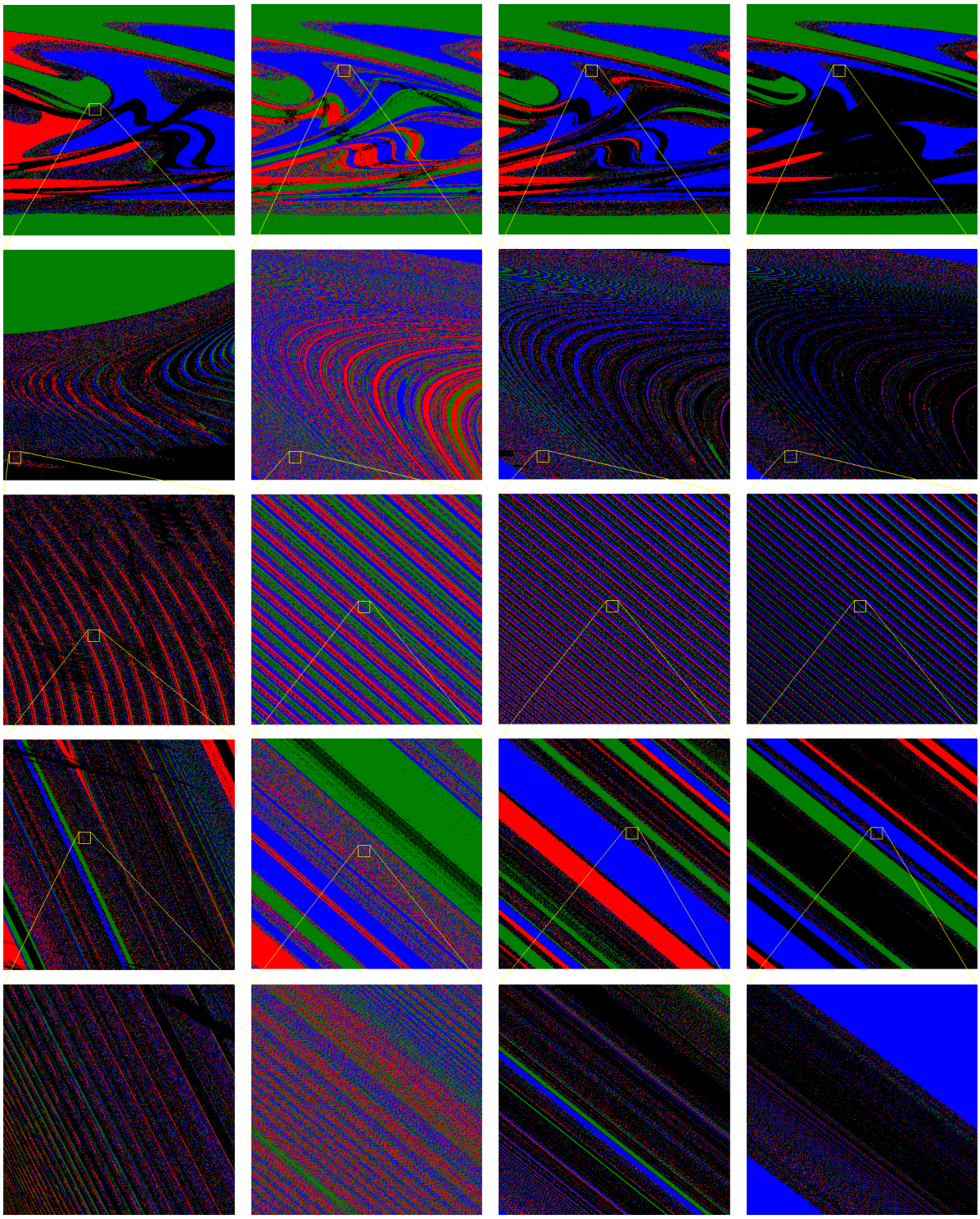

Figure 3.2 Zooming in on areas of the initial parameter space. Each post-Newtonian order (PN0, PN1, PN2, PN2.5) is represented in a column. Each row is a successive zoom of the image above it. Each zoom is 400X closer than the previous. The plots have the same features at every level of zoom, which is indicative of chaos.

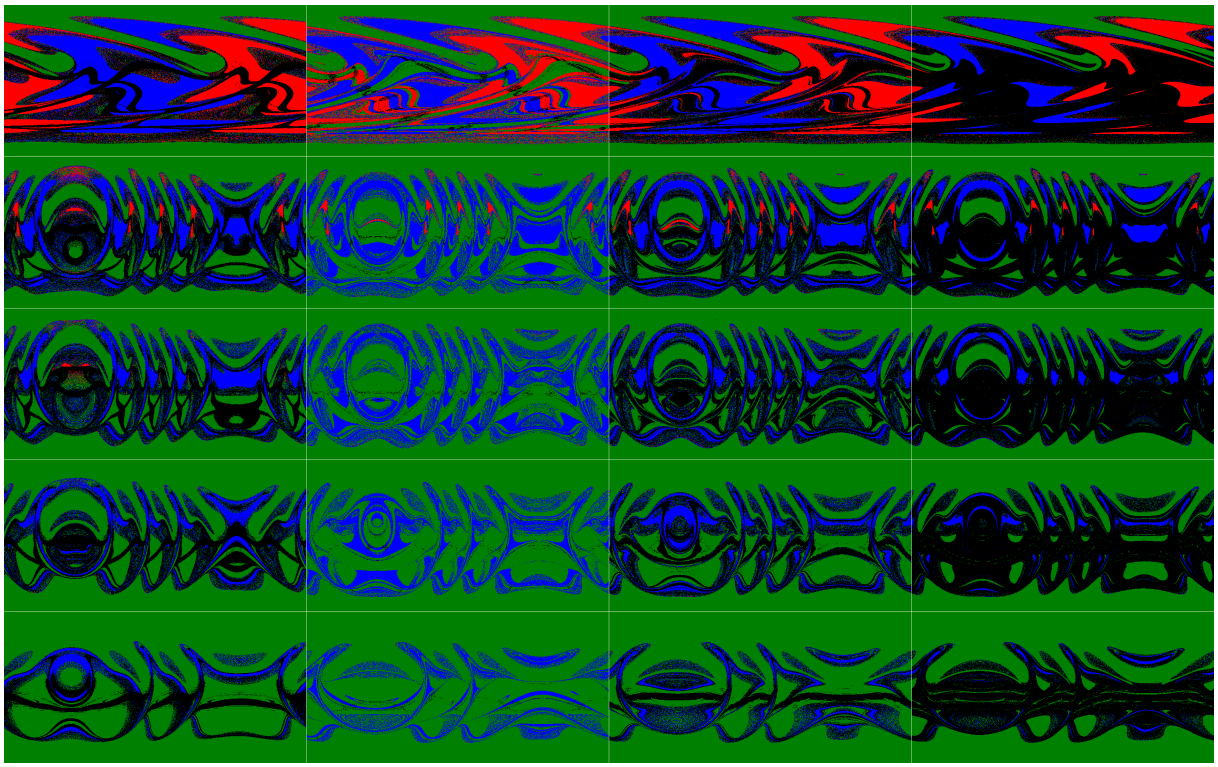

Figure 3.3 This figure shows the results of the simulations for several different values of m_1, the mass of one of the objects in the initial binary. Each row corresponds to a different value for the mass, which increases with each lower row. The value for the first row is 1, and for the lower rows is 2, 3, 5, and 10. Each column corresponds to an order of approximation to General Relativity. The first column is Newtonian gravity, and the others are PN1, PN2, and PN2.5.

Increasing the mass of one object in the binary makes it rotate more quickly, which would tend to shift the image horizontally. However, the increased mass also increases the acceleration of the third object so that the relationship between the phase of the binary and the position of the incoming object is practically independent of the mass.

One obvious effect is that there is less red in the picture as m_1 increases. The more massive the object becomes, the less likely it is that that object will be kicked out of the system.

Another effect that is easy to see and not-so-easy to understand is the symmetry that emerges around the phase angle values of $\pi/2$ and $3\pi/2$. We ought to expect symmetry in ϕ to arise simply because the binary tends toward one object with circular symmetry, but this would make the outcome completely independent of ϕ, and it would also create symmetry in the values of ρ, which we don't see at these values of m_1. However, we can see that that sort of symmetry begins to arise for values of $m_1 = 10$. The early symmetry that arises in ϕ around the specific values of $\pi/2$ and $3\pi/2$ comes from the new asymmetry of the binary and the relatively high speed of the incoming object. The angle of the binary determines whether the heavy or light side of the binary is facing the incoming object. When the incoming object is close to the binary, its velocity is four or more times the velocity of the heavy object in the binary. Because of this high speed, the rotation of the binary has little effect on the outcome. If the binary is reflected about a certain axis, the resulting interaction is roughly the same but reflected.

An additional effect is seen in the last column, at order PN2.5. The black pixels dominate the interactions more and more as the mass increases. We expect this to happen because the gravitational field of m_1 is stronger, so the third object approaching from infinity comes in more directly toward the first object and, if it doesn't just crash into it, will revolve around it very quickly and emit gravitational waves at a faster rate than it would for lower values of m_1, causing it to spiral inward more quickly and reducing the chance of escape.

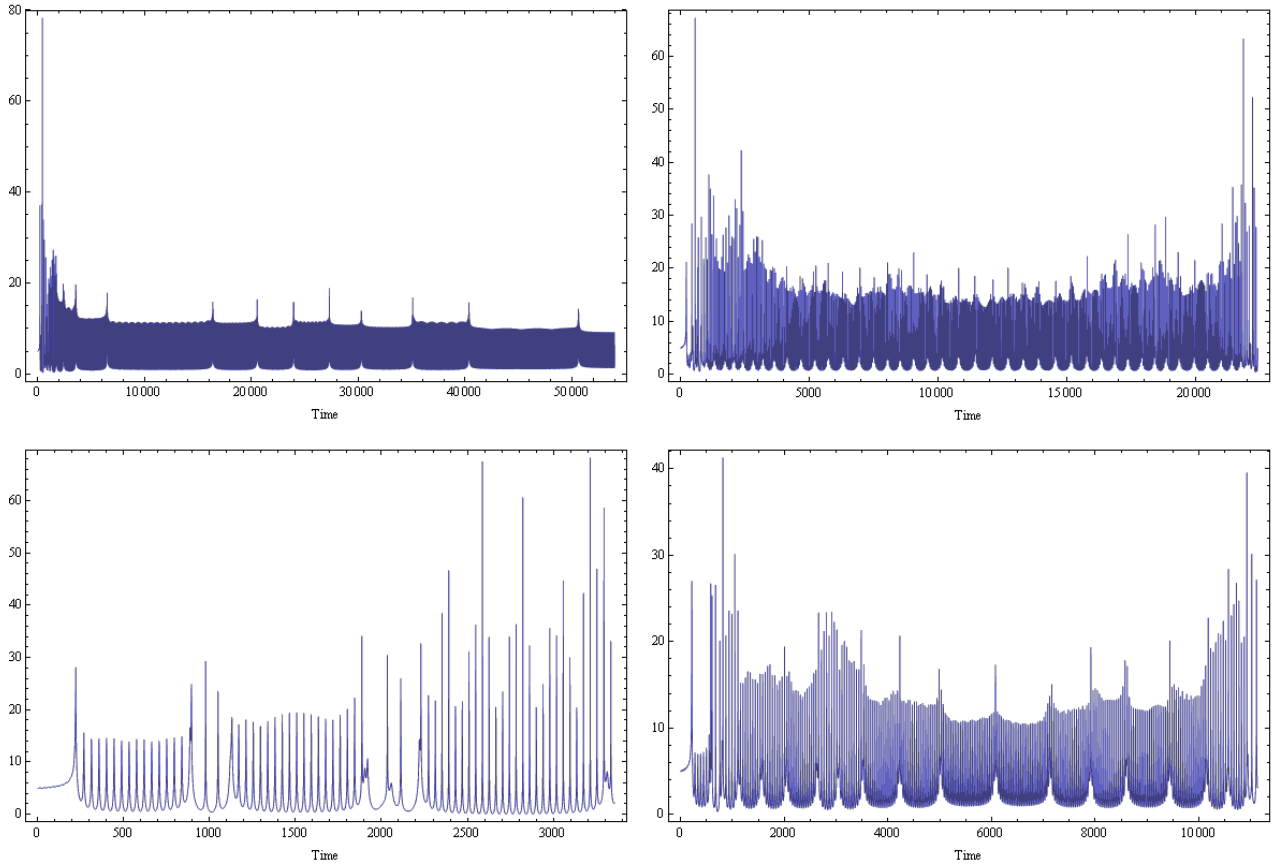

Figure 3.4 This figure shows plots of the total kinetic energy of the three-body system in certain cases where the interaction lasted for a long period of time. One run is shown from each order of approximation; they are not related. We have Newtonian gravity (top-left), first-order approximation to GR (top-right), second-order (bottom-left), and two-and-a-half order (bottom-right).

3.5 Quasi-Periodic Runs

It is interesting to examine a few of the interactions which happened to last for a very long time. We have chosen one such interaction from each order of approximation to general relativity and plotted the total kinetic energy over the course of the interaction. The runs are not related, because a long-lived interaction at one PN order often becomes much shorter at other orders. In the New-

tonian interaction (top-left), we can see three frequencies: (1) the rapid oscillation of the binary which is so quick that individual orbits cannot be distinguished at this level of zoom, (2) the long revolutions of the third body around the binary which causes a spike in the kinetic energy whenever it gets close to the binary, and (3) an intermediate frequency which is an emergent effect of three-body interactions [16]. These three frequencies still exist at higher orders, although they are less noticeable because the interactions are more complicated.

3.6 Conclusions

Our simulations indicate that the three-body problem exhibits the same properties of chaos in general relativity as it does in Newtonian gravity. We see that very small changes in the initial conditions of the system give extremely different outcomes at all available post-Newtonian orders.

Each level of post-Newtonian approximations in turn adds its own effects to the system. At first-order (PN1), the orbits begin to precess and gravity becomes repulsive for very close encounters. At second-order (PN2), higher power terms overcome the repulsion of PN1. At two-and-a-half order (PN2.5), the bodies spiral inward and collide more often than in the other orders.

These results could have important applications to black hole formations. It seems that black holes form in star clusters much more rapidly than previously thought [17, 18], and the chaotic effects of many-body systems, together with inspirals from general relativity, may be able to explain that phenomenon. Relativistic effects may also play an important role in the stability of planetary orbits. The Kepler project has found many planets [4] whose stability can be tested in general relativity with the code that our group has developed.

Appendix A

Appendix

A.1 Post-Newtonian Equations

In our simulations use a Hamiltonian-like formulation of general relativity. We made use of the ADM formulation derived by Schäfer [7] with corrections from Lousto et al. [8]. We define $\mathbf{x}_a$ to be the three-dimensional position vector in Euclidean space for an object a of mass m_a. We define $\mathbf{r}_{ab} = \mathbf{x}_a - \mathbf{x}_b$, $r_{ab} = |\mathbf{r}_{ab}|$, and $\mathbf{n}_{ab} = \mathbf{r}_{ab}/r_{ab}$. We define $\mathbf{p}_a$ to be the momentum of object a. Assuming $(v/c)^2$ is small and using a perturbation approach, the Hamiltonian becomes

$$H = H_N + \frac{1}{c^2}H_{PN1} + \frac{1}{c^4}H_{PN2} + \frac{1}{c^5}H_{PN2.5}. \tag{A.1}$$

where H_N is the Newtonian Hamiltonian and H_{PN1}, H_{PN2}, and $H_{PN2.5}$ are successive approximations to General Relativity. The equations of motion are

$$(\dot{x}_a^i)_n = \frac{\partial H_n}{\partial p_a^i}, \tag{A.2}$$

$$(\dot{p}_a^i)_n = -\frac{\partial H_n}{\partial x_a^i}, \tag{A.3}$$

$$\dot{\mathbf{x}}_a = (\dot{\mathbf{x}}_a)_0 + (\dot{\mathbf{x}}_a)_1 + (\dot{\mathbf{x}}_a)_2 + (\dot{\mathbf{x}}_a)_{2.5}, \tag{A.4}$$

$$\dot{\mathbf{p}}_a = (\dot{\mathbf{p}}_a)_0 + (\dot{\mathbf{p}}_a)_1 + (\dot{\mathbf{p}}_a)_2 + (\dot{\mathbf{p}}_a)_{2.5}, \tag{A.5}$$

where i labels the axis and a labels the object. We now proceed to write out each order of approximation of the Hamiltonian assuming $G = 1$ and $c = 1$.

$$H_N = \frac{1}{2}\sum_a \frac{p_a^2}{m_a} - \frac{1}{2}\sum_{a,b\neq a} \frac{m_a m_b}{r_{ab}} \tag{A.6}$$

$$\begin{aligned} H_{PN1} = -\frac{1}{8}\sum_a m_a \left(\frac{p_a^2}{m_a^2}\right)^2 - \frac{1}{4}\sum_{a,b\neq a} \frac{m_a m_b}{r_{ab}} \left\{ 6\frac{p_a^2}{m_a^2} - 7\frac{\mathbf{p}_a \cdot \mathbf{p}_b}{m_a m_b} - \frac{(\mathbf{n}_{ab}\cdot\mathbf{p}_a)(\mathbf{n}_{ab}\cdot\mathbf{p}_b)}{m_a m_b} \right\} \\ + \frac{1}{2}\sum_{a,b\neq a,c\neq a} \frac{m_a m_b m_c}{r_{ab} r_{ac}} \end{aligned} \tag{A.7}$$

$$
\begin{aligned}
H_{PN2} = {} & \frac{1}{16}\sum_a m_a\left(\frac{p_a^2}{m_a^2}\right)^3 + \frac{1}{16}\sum_{a,b\neq a}\frac{m_a m_b}{r_{ab}}\left\{10\left(\frac{p_a^2}{m_a^2}\right)^2 - 11\frac{p_a^2 p_b^2}{m_a^2 m_b^2} - 2\frac{(\mathbf{p}_a\cdot\mathbf{p}_a)^2}{m_a^2 m_b^2} + 10\frac{p_a^2(\mathbf{n}_{ab}\cdot\mathbf{p}_b)^2}{m_a^2 m_b^2}\right. \\
& \left. - 12\frac{(\mathbf{p}_a\cdot\mathbf{p}_b)(\mathbf{n}_{ab}\cdot\mathbf{p}_a)(\mathbf{n}_{ab}\cdot\mathbf{p}_b)}{m_a^2 m_b^2} - 3\frac{(\mathbf{n}_{ab}\cdot\mathbf{p}_a)^2(\mathbf{n}_{ab}\cdot\mathbf{p}_b)^2}{m_a^2 m_b^2}\right\} \\
& + \frac{1}{8}\sum_{a,b\neq a,c\neq a}\frac{m_a m_b m_c}{r_{ab} r_{ac}}\left\{18\frac{p_a^2}{m_a^2} + 14\frac{p_b^2}{m_b^2} - 2\frac{(\mathbf{n}_{ab}\cdot\mathbf{p}_b)^2}{m_b^2} - 50\frac{\mathbf{p}_a\cdot\mathbf{p}_b}{m_a m_b} + 17\frac{\mathbf{p}_b\cdot\mathbf{p}_c}{m_b m_c}\right. \\
& \left. - 14\frac{(\mathbf{n}_{ab}\cdot\mathbf{p}_a)(\mathbf{n}_{ab}\cdot\mathbf{p}_b)}{m_a m_b} + 14\frac{(\mathbf{n}_{ab}\cdot\mathbf{p}_b)(\mathbf{n}_{ab}\cdot\mathbf{p}_c)}{m_b m_c} + \mathbf{n}_{ab}\cdot\mathbf{n}_{ac}\frac{(\mathbf{n}_{ab}\cdot\mathbf{p}_b)(\mathbf{n}_{ac}\cdot\mathbf{p}_c)}{m_b m_c}\right\} \\
& + \frac{1}{8}\sum_{a,b\neq a,c\neq a}\frac{m_a m_b m_c}{r_{ab}^2}\left\{2\frac{(\mathbf{n}_{ab}\cdot\mathbf{p}_a)(\mathbf{n}_{ac}\cdot\mathbf{p}_c)}{m_a m_c} + 2\frac{(\mathbf{n}_{ab}\cdot\mathbf{p}_b)(\mathbf{n}_{ac}\cdot\mathbf{p}_c)}{m_a m_c} + 5\mathbf{n}_{ab}\cdot\mathbf{n}_{ac}\frac{p_c^2}{m_c^2}\right. \\
& \left. - \mathbf{n}_{ab}\cdot\mathbf{n}_{ac}\frac{(\mathbf{n}_{ac}\cdot\mathbf{p}_c)^2}{m_c^2} - 14\frac{(\mathbf{n}_{ab}\cdot\mathbf{p}_c)(\mathbf{n}_{ac}\cdot\mathbf{p}_c)}{m_c^2}\right\} + \frac{1}{4}\sum_{a,b\neq a}\frac{m_a^2 m_b}{r_{ab}^2}\left\{\frac{p_a^2}{m_a^2} + \frac{p_b^2}{m_b^2} - 2\frac{\mathbf{p}_a\cdot\mathbf{p}_b}{m_a m_b}\right\} \\
& + \frac{1}{2}\sum_{a,b\neq a,c\neq a,b}\frac{m_a m_b m_c}{(r_{ab}+r_{bc}+r_{ca})^2}(n_{ab}^i + n_{ac}^i)(n_{ab}^j + n_{cb}^j)\left\{8\frac{p_{ai}p_{cj}}{m_a m_c} - 16\frac{p_{aj}p_{ci}}{m_a m_c} + 3\frac{p_{ai}p_{bj}}{m_a m_b}\right. \\
& \left. + 4\frac{p_{ci}p_{cj}}{m_c^2} + \frac{p_{ai}p_{aj}}{m_a^2}\right\} + \frac{1}{2}\sum_{a,b\neq a,c\neq a,b}\frac{m_a m_b m_c}{(r_{ab}+r_{bc}+r_{ca})r_{ab}}\left\{8\frac{\mathbf{p}_a\cdot\mathbf{p}_c - (\mathbf{n}_{ab}\cdot\mathbf{p}_a)(\mathbf{n}_{ab}\cdot\mathbf{p}_c)}{m_a m_c}\right. \\
& \left. - 3\frac{\mathbf{p}_a\cdot\mathbf{p}_b - (\mathbf{n}_{ab}\cdot\mathbf{p}_a)(\mathbf{n}_{ab}\cdot\mathbf{p}_b)}{m_a m_b} - 4\frac{p_c^2 - (\mathbf{n}_{ab}\cdot\mathbf{p}_c)^2}{m_c^2} - \frac{p_a^2 - (\mathbf{n}_{ab}\cdot\mathbf{p}_a)^2}{m_a^2}\right\} - \frac{1}{2}\sum_{a,b\neq a,c\neq b}\frac{m_a^2 m_b m_c}{r_{ab}^2 r_{bc}} \\
& - \frac{1}{4}\sum_{a,b\neq a,c\neq a}\frac{m_a m_b m_c^2}{r_{ab} r_{ac}^2} + \frac{1}{2}\sum_{a,b\neq a}\frac{m_a^3 m_b}{r_{ab}^3} - \frac{3}{4}\sum_{a,b\neq a,c\neq a}\frac{m_a^2 m_b m_c}{r_{ab}^2 r_{ac}} - \frac{3}{8}\sum_{a,b\neq a,c\neq a,b}\frac{m_a^2 m_b m_c}{r_{ab} r_{ac} r_{bc}} \\
& + \frac{3}{8}\sum_{a,b\neq a}\frac{m_a^2 m_b^2}{r_{ab}^3} - \frac{1}{64}\sum_{a,b\neq a,c\neq a,b}\frac{m_a^2 m_b m_c}{r_{ab}^3 r_{ac}^3 r_{bc}}\left\{18 r_{ab}^2 r_{ac}^2 - 60 r_{ab}^2 r_{bc}^2 - 24 r_{ab}^2 r_{ac}(r_{ab}+r_{bc})\right. \\
& \left. + 60 r_{ab} r_{ac} r_{bc}^2 + 56 r_{ab}^3 r_{bc} - 72 r_{ab} r_{bc}^3 + 35 r_{bc}^4 + 6 r_{ab}^4\right\} - \frac{1}{4}\sum_{a,b\neq a}\frac{m_a^2 m_b^2}{r_{ab}^3}. \qquad \text{(A.8)}
\end{aligned}
$$

$H_{PN2.5}$ contains terms which include gravitational wave emission. Because of our choice of units, we use the version of $H_{PN2.5}$ given by Galaviz [10].

$$
H_{PN2.5} = \frac{1}{45}\dot{\chi}_{(4)ij}(\mathbf{x}_{a'}, \mathbf{p}_{a'}; t)\chi_{(4)ij}(\mathbf{x}_a, \mathbf{p}_a), \qquad \text{(A.9)}
$$

where

$$\chi_{(4)ij}(\mathbf{x}_a,\mathbf{p}_a)=\sum_a\frac{2}{m_a}\big((\mathbf{p}_a\cdot\mathbf{p}_a)\delta_{ij}-3p_{ai}p_{aj}\big)+\sum_{a,b\neq a}\frac{m_am_b}{r_{ab}}\big(3n_{abi}n_{abj}-\delta_{ij}\big), \tag{A.10}$$

and

$$\begin{aligned}\dot\chi_{(4)ij}(\mathbf{x}_{a'},\mathbf{p}_{a'})=&\sum_{a'}\frac{2}{m_{a'}}\Big[2\big(\dot{\mathbf{p}}_{a'}\cdot\mathbf{p}_{a'}\big)\delta_{ij}-3(\dot p_{a'i}p_{a'j}+p_{a'i}\dot p_{a'j})\Big]\\&+\sum_{a',b'\neq a'}\frac{m_{a'}m_{b'}}{r_{a'b'}^2}\Big[3(\dot r_{a'b'i}n_{a'b'j}+n_{a'b'i}\dot r_{a'b'j})+(\mathbf{n}_{a'b'}\cdot\dot{\mathbf{r}}_{a'b'})(\delta_{ij}-9n_{a'b'i}n_{a'b'j})\Big],\end{aligned} \tag{A.11}$$

approximating the derivatives of x and p with the PN1 equations of motion:

$$(\dot{\mathbf{x}}_a)_1=-\frac{p_a^2}{2m_a^3}\mathbf{p}_a-\frac{1}{2}\sum_{b\neq a}\frac{1}{r_{ab}}\left(6\frac{m_b}{m_a}\mathbf{p}_a-7\mathbf{p}_b-(\mathbf{n}_{ab}\cdot\mathbf{p}_b)\mathbf{n}_{ab}\right) \tag{A.12}$$

$$\begin{aligned}(\dot{\mathbf{p}}_a)_1=&-\frac{1}{2}\sum_{b\neq a}\left[3\frac{m_b}{m_a}p_a^2-7(\mathbf{p}_a\cdot\mathbf{p}_b)-3(\mathbf{n}_{ab}\cdot\mathbf{p}_a)(\mathbf{n}_{ab}\cdot\mathbf{p}_a)\right]\frac{\mathbf{n}_{ab}}{r_{ab}^2}\\&+\sum_{b\neq a,c\neq a}\frac{m_am_bm_c}{r_{ab}^2r_{ac}}\mathbf{n}_{ab}+\sum_{b\neq a,c\neq b}\frac{m_am_bm_c}{r_{ab}^2r_{bc}}\mathbf{n}_{ab}-\frac{1}{2}\sum_{a\neq b}\left[\frac{(\mathbf{n}_{ab}\cdot\mathbf{p}_b)\mathbf{p}_a+(\mathbf{n}_{ab}\cdot\mathbf{p}_a)\mathbf{p}_b}{r_{ab}^2}\right].\end{aligned} \tag{A.13}$$

The primed variables in the equation for $\dot\chi$ are unaffected by the partial derivatives in the Hamiltonian equations, so the 2.5PN equations of motion are

$$(\dot{\mathbf{x}}_a)_{2.5}=\frac{1}{45}\dot\chi_{(4)ij}(\mathbf{x}_a,\mathbf{p}_a;(\dot{\mathbf{x}}_a)_1,(\dot{\mathbf{p}}_a)_1,t)\frac{\partial}{\partial\mathbf{p}_a}\chi_{(4)ij}(\mathbf{x}_a,\mathbf{p}_a) \tag{A.14}$$

$$(\dot{\mathbf{p}}_a)_{2.5}=-\frac{1}{45}\dot\chi_{(4)ij}(\mathbf{x}_a,\mathbf{p}_a;(\dot{\mathbf{x}}_a)_1,(\dot{\mathbf{p}}_a)_1,t)\frac{\partial}{\partial\mathbf{x}_a}\chi_{(4)ij}(\mathbf{x}_a,\mathbf{p}_a) \tag{A.15}$$

Bibliography

[1] J. Barrow-Green, *Poincare and the Three Body Problem* (American Mathematical Society, 1996).

[2] M. J. Valtonen and H. Karttunen, *The three-body problem* (Cambridge University Press, New York, 1996).

[3] A. Morbidelli, *Modern Celestial Mechanics* (CRC Press, 2002).

[4] NASA, *Kepler*, 2015, http://kepler.nasa.gov (accessed March 30, 2015).

[5] P. Boyd and S. McMillan, "Chaotic scattering in the gravitational three-body problem," Chaos **3,** 507–524 (1993).

[6] D. Tanner, "Chaotic Scattering In The 2nd Post-Newtonian Order Gravitational Three-Body Problem,", Brigham Young University Senior Thesis, 2007.

[7] Schäfer, Gerhard, "Three-body Hamiltonian in General Relativity," Phys. Lett. A **123,** 336–339 (1987).

[8] C. Lousto and H. Nakano, "Three-body equations of motion in successive post-Newtonian approximations," Classical and Quantum Gravity 25 (2008).

[9] J. Campbell, "Chaos In The Post-Newtonian Gravitational Three-Body Problem,", Brigham Young University Senior Thesis, 2008.

[10] Galaviz Vilchis, Juan Pablo, Ph.D. thesis, Friedrich-Schiller-Universitat Jena, 2011.

[11] Jaranowski, Piotr and Schäfer, Gerhard, "Radiative 3.5 postNewtonian ADM Hamiltonian for many body point - mass systems," Phys.Rev. **D55,** 4712–4722 (1997).

[12] Schäfer, Gerhard, "Post-Newtonian methods: Analytic results on the binary problem," Fundam.Theor.Phys. **162,** 167–210 (2011).

[13] A. C. Hindmarsh, "LSODE and LSODI, Two New Initial Value Ordinary Differential Equation Solvers," acm-signum newsletter **15,** 10–11 (1980).

[14] L. R. Petzold, "Automatic Selection of Methods for Solving Stiff and Nonstiff Systems of Ordinary Differential Equations," siam j. sci. stat. comput. **4,** 136–148 (1983).

[15] M. Maggiore, "Gravitational Waves. Vol. 1: Theory and Experiments," (2007).

[16] W. H. Jefferys and J. Moser, "Quasi-periodic solutions for the three-body problem," The Astronomical Journal **71,** 568 (1966).

[17] M. Colpi, "Massive Binary Black Holes in Galactic Nuclei and Their Path to Coalescence," in *The Physics of Accretion onto Black Holes*, Vol. 49 of *Space Sciences Series of ISSI*, M. Falanga, T. Belloni, P. Casella, M. Gilfanov, P. Jonker, and A. King, eds., (Springer New York, 2015), pp. 189–221.

[18] M. Volonteri, "Formation of supermassive black holes," The Astronomy and Astrophysics Review **18,** 279–315 (2010).

Index